Carbonate Complexation of Mn²⁺ in the Aqueous Phase: Redox Behavior and Ligand Binding Modes by Electrochemistry and EPR Spectroscopy

Jyotishman Dasgupta,[†] **Alexei M. Tyryshkin,**[‡] **Yuri N. Kozlov,**[§] **Vyacheslav V. Klimov,**[§] **and G. Charles Dismukes*,**[†]

Hoyt Laboratory, Department of Chemistry, and Department of Electrical Engineering, Princeton University, Princeton, New Jersey 08544, and Russian Academy of Sciences, Institute of Basic Biological Problems, Pushchino, Moscow region 142290, Russia

The chemical speciation of Mn²⁺ within cells is critical for its transport, availability, and redox properties. Herein we investigate the redox behavior and complexation equilibria of Mn²⁺ in aqueous solutions of bicarbonate by voltammetry and electron paramagnetic resonance (EPR) spectroscopy and discuss the implications for the uptake of Mn²⁺ by mangano-cluster enzymes such as photosystem II (PSII). Both the electrochemical reduction of Mn²⁺ to Mn⁰ at an Hg electrode and EPR (in the absence of a polarizing electrode) revealed the formation of 1:1 and 1:2 Mn–(bi)carbonate complexes as a function of Mn²⁺ and bicarbonate concentrations. Pulsed EPR spectroscopy, including ENDOR, ESEEM, and 2D-HYSCORE, were used to probe the hyperfine couplings to ¹H and ¹³C nuclei of the ligand(s) bound to Mn²⁺. For the 1:2 complex, the complete ¹³C hyperfine tensor for one of the (bi)carbonate ligands was determined and it was established that this ligand coordinates to Mn²⁺ in bidentate mode with a ¹³C–Mn distance of 2.85 ± 0.1 Å. The second (bi)carbonate ligand in the 1:2 complex coordinates possibly in monodentate mode, which is structurally less defined, and its ¹³C signal is broad and unobservable. ¹H ENDOR reveals that 1–2 water ligands are lost upon binding of one bicarbonate ion in the 1:1 complex while 3–4 water ligands are lost upon forming the 1:2 complex. Thus, we deduce that the dominant species above 0.1 M bicarbonate concentration is the 1:2 complex, $[Mn(CO_3)(HCO_3)(OH_2)_3]^-$.

I. Introduction

The bioavailability of essential trace metal ions (Fe^{2+}, Mn^{2+}, Cu^{2+}, Zn^{2+}, Cd^{2+}, and Ni^{2+}) in ecosystems is governed by their complexation equilibria with naturally occurring ligands that exist in open oceans and at soil–water interfaces.[1] Inorganic ligands such as carbonate/bicarbonate ions, derived from CO_2 and soluble carbonate minerals, play a dominant role in metal ion speciation in marine ecosystems. This speciation leads to significant changes in the redox potentials of metal ions and thus influences the biogeochemical cycles of elements on a macroscopic scale. The carbonate system ($CO_2/HCO_3^-/CO_3^{2-}$) is particularly versatile in this regard for several reasons. First, it readily chelates metal ions and also forms μ-carbonato bridges leading to oligomeric clusters $M_x(CO_3)_y$ in solution that are in equilibrium with insoluble mineral forms, for example, siderite ($FeCO_3$), rhodochrosite ($MnCO_3$), and so forth.[2] Second, the amphoteric properties of bicarbonate ($pK_a = 6.3$, 10.5) straddle the pH of the oceans, which enables bicarbonate to drive the metal ion speciation by serving as either an acid or a base. The metal–ligand speciation goes together with the changes in redox potential, which is exploited by organisms for the selective uptake, intracellular delivery, and redox poising of metal ions within functional sites in macromolecules.[3]

An example of such a macromolecule that uses bicarbonate for metal cluster assembly is photosystem II (PSII), a multi-subunit membrane-spanning protein complex required for oxygenic photosynthesis.[4,5] A domain within the PSII, known as the water oxidizing complex (WOC), harbors an inorganic Mn-based catalyst that oxidizes water to dioxygen. Early biochemical studies (reviewed in ref 6) had indicated that bicarbonate is involved in functioning and/or assembly of the WOC inorganic core. In the last decade, several types of studies have indicated a specific role for bicarbonate in functioning of the WOC. The rate of electron transfer from the Mn^{2+} ion to apo-PSII is accelerated in the presence of bicarbonate.[7] Bicarbonate increases the affinity of the Mn^{2+} to apo-PSII by forming a ternary complex and thus accelerates the rate of light-driven assembly of the inorganic core during its biogenesis or repair, a process known as photoactivation.[8] A recent crystal structure of PSII-WOC from *T. elongutus* at 3.5-Å resolution has proposed the atomic structure to consist of an Mn_4CaO_4 core, having four oxo/hydroxo/aquo ligands bridging the metals to form a cubical Mn_3CaO_4 subcore that is bridged to the fourth external Mn atom at one of the corner oxos,[4] although this model remains debated.[9,10] The XRD data provides evidence for the presence of a planar ligand in the active site, suggested to be HCO_3^-/CO_3^{2-} or NO_3^- that is positioned between Ca and the external Mn atom. Site-directed mutagenesis of the protein residue that defines the binding site has provided some support for a possible functional bicarbonate at this location.[4,11] Geochemical evidence has led to the proposal that Mn–bicarbonate clusters may have played the seminal role in the evolution of the first oxygenic phototroph from an ancestral anoxygenic bacterial precursor.[12,13] This hypothesis has been

* Corresponding author. E-mail: dismukes@princeton.edu.
† Hoyt Laboratory, Department of Chemistry, Princeton University.
‡ Department of Electrical Engineering, Princeton University.
§ Russian Academy of Sciences.

supported by evidence from site-directed mutants of an anoxygenic purple bacterial reaction center, which were engineered to photooxidize Mn^{2+} when bicarbonate is added to the media.[14,15]

The stoichiometry and stability constants for the formation of Mn^{2+}−bicarbonate complexes have been studied previously by pH potentiometric titrations as a function of bicarbonate concentration. In these measurements, the molecularity of the complexes were assumed based on simple chemical principles of charge balance. Mn−bicarbonate complexes have also been the subject of scrutiny by biologists owing to their efficiency in catalyzing the dismutation of hydrogen peroxide, also known as its "pseudo-catalase" activity.[16,17] The observed pseudo-catalase rates have been used as an indirect probe for the molecularity of these complexes. On this basis it has been reported that these complexes can form dimers in solution with bicarbonate, although no direct structural evidence has been presented.[18−20] Previously we have reported direct electrochemical measurements of the oxidation potential for the conversion of Mn^{2+} to Mn^{3+} in the presence of bicarbonate.[21] This suggested the presence of dimanganese or oligomeric forms in solution. No structure-sensitive spectroscopic methods were used in any of the mentioned studies to determine the speciation of Mn^{2+} in bicarbonate solution.

Herein, we characterize the equilibrium constants and chemical structures of Mn^{2+}−bicarbonate complexes that form in aqueous solution using EPR and potentiometric titration. Cyclic voltammetry on the reduction of Mn^{2+} at varied bicarbonate concentrations is used to determine the metal/ligand stoichiometry of the Mn^{2+}−bicarbonate complexes. EPR spectroscopy is used to confirm the ligand stoichiometry and to measure the ligand field symmetry of the Mn^{2+} complexes.[22,23] Hyperfine couplings to ligand nuclei (^{13}C and ^{1}H) obtained from ENDOR and ESEEM provides us the information about coordination geometry and distances to the ligands.[24−26]

II. Experimental Section

Solutions of Mn^{2+} and $NaHCO_3$ were prepared by mixing stock solutions of 10 mM $MnClO_4 \cdot 6H_2O$ (Sigma) and freshly prepared 10−300 mM $NaHCO_3$ (Sigma-Aldrich). $NaH^{13}CO_3$ (99% pure) powder from Cambridge Isotopes Laboratory Inc. was used to prepare samples with ^{13}C-labeled bicarbonate. In all of the preparations, the pH of the solution was 8.3 (self-buffered by $NaHCO_3$).

Mn^{2+}−bicarbonate solutions are quasi-stable at room temperature, with a white precipitate slowly forming upon standing because of the formation of insoluble $MnCO_{3(s)}$. At the low Mn^{2+} concentrations (<0.25 mM) used in our voltammetry experiments, a visible precipitate developed within 2−3 h, which was sufficient time to perform the experiment. Freshly mixed solutions were always used in these experiments. At high concentrations of Mn^{2+} (1 mM) and HCO_3^- (200−300 mM) as used in room-temperature EPR experiments, the precipitate forms within minutes, that is, on the time scale of the experiment. Thus, the Mn^{2+} EPR signal was recorded at different time points after sample mixing and, the signal at time point zero (i.e., immediately after mixing and before precipitation starts) was reconstructed by back extrapolation.

For frozen-solution EPR experiments, the samples were prepared in a (1:3) CH_3OH/H_2O solvent mixture,[27] with methanol added as a glass-forming agent.[54] Stock solutions of $MnClO_4 \cdot 6H_2O$ and $NaHCO_3$ in (1:3) CH_3OH/H_2O were mixed and immediately frozen in liquid N_2 to avoid any loss of Mn^{2+} due to precipitation. $KHCO_3$ (in 1:3 CH_3OH/H_2O) was also

tested instead of $NaHCO_3$ to prepare samples, although because of poor glass formation upon freezing it could not be used for any quantitative measurements. Calibrated EPR tubes and identical volumes of the samples were used to allow quantitative comparison. In separate titration experiments (see Figure S3 in the Supporting Information), we confirmed that addition of methanol and freezing to low temperatures do not significantly alter the Mn^{2+} speciation equilibrium from that observed at room temperature.

Voltammetry experiments were done with a standard potentiostat (polarographic analyzer model PA-3; LP, Praha) using a three-electrode cell as described earlier.[28] In Mn^{2+} reduction experiments, the working electrode was a hanging mercury drop with a diameter of 0.72 mm, which was renewed before each measurement. A Pt plate (1 × 1 cm²) was used as a counter electrode, while a saturated calomel electrode formed the reference electrode. The measured wave potentials were then recalculated versus the normal hydrogen electrode (NHE). The scan rate was 50 mV/sec.

CW EPR spectra were collected using a Bruker ESP300e spectrometer. Room-temperature aqueous solution spectra were measured using a flat cell in a standard TM102 cavity at microwave (MW) frequency, 9.69 GHz. Frozen-solution experiments (77 K) were done using a liquid N_2 finger dewar in a TE011 cavity at 9.14 GHz. The MW power setting was 0.2 mW, the modulation amplitude was 5−10 G, and the modulation frequency was 100 kHz.

Pulsed EPR experiments were performed using an X-band Bruker Elexsys580 spectrometer. The sample temperature was set in the 5−10 K range using a liquid helium flow cryostat CF935 from Oxford Instruments. In all of the electron spin−echo (ESE)-based experiments, durations of the $\pi/2$ and π pulses were set to 16 and 32 ns, respectively. Field-sweep ESE-detected EPR spectra were collected using a two-pulse echo sequence, $\pi/2 - \tau - \pi - \tau -$ echo, with fixed interpulse delay $\tau = 400$ ns; the integrated echo intensity was detected while sweeping the magnetic field. For two-pulse electron spin echo envelope modulation (ESEEM) experiments, $\pi/2 - \tau - \pi - \tau -$ echo, the echo intensity was measured as a function of τ, starting from an initial 100 ns and incrementing with 16-ns steps. The 2D HYSCORE experiment, $\pi/2 - \tau - \pi/2 - t_1 - \pi - t_2 - \pi/2 - \tau -$ echo, was recorded at fixed $\tau = 176$ ns and with t_1 and t_2 incremented independently from 200 ns by 24-ns steps. For Mims ENDOR experiments, the stimulated echo pulse sequence, $\pi/2 - \tau - \pi/2 - T - \pi/2 - \tau -$ echo, was used with nonselective microwave pulses (16 ns) and with $\tau = 200$ ns. A selective RF pulse (50 μs) of variable frequency was applied during a time interval, T. Whenever necessary, phase cycling was done to eliminate unwanted echo signals.

Data processing and analysis was done with WINEPR software (Bruker BioSpin) and MATLAB 6.0 (MathWorks Inc.). Prior to Fourier transformation, the 1D ESEEM time domains were normalized to unity background by fitting the relaxation decays with a smoothing spline function followed by division of the experimental time domain by the fitted baseline decay. The 2D HYSCORE time-domain traces were baseline-corrected in two dimensions with a suitable polynomial function. Appodization with a Hamming window and zero filling was performed prior to Fourier transformation (FT). All of the 1D frequency-domain ESEEM spectra shown are the phase-corrected cosine part of the FT. The 2D HYSCORE spectrum is presented in absolute mode after 2D-FT. The ENDOR spectra shown were normalized to the echo signal intensity in the absence of radio frequency.

Mn^{2+} Speciation in Aqueous Solutions of Carbonate

J. Phys. Chem. B, Vol. 110, No. 10, 2006 **5101**

EPR Theory and Simulations. Mn^{2+} has five unpaired electrons (3d^5), and its electronic ground state in the octahedral ligand field has the high-spin configuration (^{6}S) with electron spin $S = 5/2$. The spin-Hamiltonian for Mn^{2+} is represented in the form

$$H = g\beta B_0 S_Z + \vec{S}\cdot\hat{D}\cdot\vec{S} + A_{Mn}\cdot\vec{S}\cdot\vec{I} +$$
$$\sum_i (\vec{S}\cdot\hat{A}_{(i)}\cdot\vec{I}^{(i)} + g_n\beta_n B_0 I_Z^{(i)}) \quad (1)$$

Here the first term describes the electron Zeeman interaction; g is electron g-factor, β is the Bohr magneton, B_0 is the magnetic field applied along the Z axis in the laboratory coordinate system. The g factor is assumed to be isotropic, which is a good approximation for Mn^{2+} in the octahedral ligand field at X-band frequency. The second term is a zero-field splitting (ZFS) interaction described by a traceless tensor, $\hat{D}$. It results from spin−orbit interaction of the ^{6}S ground state with excited electronic states, and its magnitude and symmetry depend on both the strength and symmetry of the ligand field around Mn^{2+}. The tensor, D, is usually described by two parameters, D and E, representing the axial and rhombic ZFS components, respectively. The third term is the magnetic hyperfine interaction with the ^{55}Mn nuclear spin ($I = 5/2$); because Mn^{2+} has a half-filled 3d^5 configuration, the hyperfine coupling, A_{Mn}, is isotropic to a good approximation. The last term represents the hyperfine interaction, $\hat{A}_{(i)}$, and the nuclear Zeeman interaction (g_n is the nuclear g-factor, β_n is the nuclear magneton) summed over all magnetic nuclei (i) in the coordination sphere of Mn^{2+}. In our case, the possible ligands to Mn^{2+} are HCO$_3^-$, CO$_3^{2-}$, and H$_2$O.

All of the EPR experiments described in this work were analyzed using the spin-Hamiltonian (1); however not all of its terms are equally important in describing each experiment. Because the electron Zeeman interaction $\gg (\hat{D}$ and $A_{Mn}) \gg (\hat{A}_{(i)}$ and nuclear Zeeman interactions), a perturbation approach can be applied conveniently. The field-sweep EPR spectra can be described fully by the first three terms of the spin-Hamiltonian, and accordingly only the electron g-tensor, ZFS coupling, and ^{55}Mn hyperfine parameters are obtainable from these spectra. The weak hyperfine couplings with ligand nuclei are usually unresolved in the EPR spectra and contribute only to the EPR line width.

ESEEM and ENDOR experiments were performed to resolve weak hyperfine couplings from ligand nuclei. Recent work by Astashkin et al. has considered the case of high-spin systems interacting with a nuclear spin $I = 1/2$.[29] It has been demonstrated that the position and intensity of the nuclear transitions in ESEEM/ENDOR spectra depend mostly on the ZFS interaction and the ligand hyperfine coupling. The position of the sum combination line (ν_σ) in ESEEM spectra has been found to be most sensitive and described by the product of two parameters: the ZFS coupling, D, and the anisotropic part of hyperfine coupling tensor, T. Thus, D and T can in principle be derived from the observed shift in ν_σ, and the isotropic part of the hyperfine tensor can then be estimated from the position of other lines in the spectra.[29] We found in practice that the situation is more complex, and we were only able to extract these parameters after analyzing the correlation peaks in the 2D HYSCORE spectra. In this analysis and in the spectral simulations, we used the analytical expressions published by Astashkin et al. for nuclear transition frequencies in a high-spin electron system. All of the spectral simulation programs for ESEEM, ENDOR, and HYSCORE were written using MATLAB (the programs are available on request). ESEEM and HYSCORE
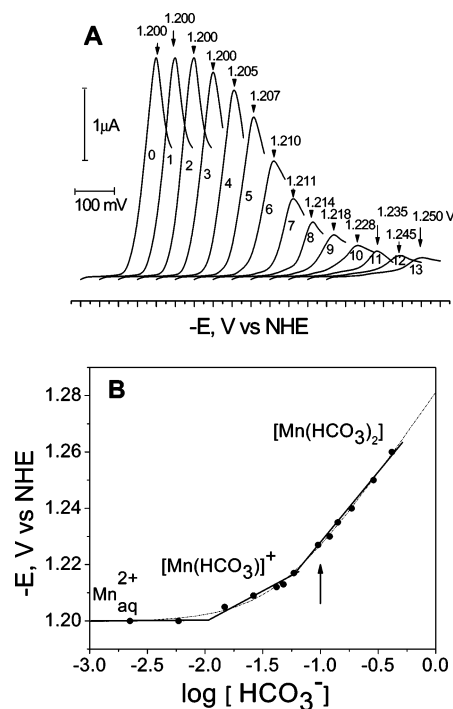

Figure 1. (A) Voltage−current curves of Mn^{2+} (0.25 mM MnSO$_4$) reduction in aqueous solutions of 0.1 M LiClO$_4$ at different concentrations of added NaHCO$_3$: 0 mM (curve 0); 2.91 mM (curve 1); 5.81 mM (curve 2); 8.72 mM (curve 3); 17.4 mM (curve 4); 26.2 mM (curve 5); 37.8 mM (curve 6); 49.4 mM (curve 7); 78.5 mM (curve 8); 113 mM (curve 9); 157 mM (curve 10); 209 mM (curve 11); 296 mM (curve 12); 381 mM (curve 13). The curves are shifted on the x axis for clarity. The peak potentials are indicated at the top of each curve. (B) Peak potentials (E_p) from A are plotted as a logarithmic function of bicarbonate concentration (see Figure 1A for experimental conditions). The data fits are shown using the Lingane (solid line) and DeFord− Hume (dashed line) equations; in the later case the speciation model of eq 7 was assumed. Also shown are the major species at each concentration range. The arrow shows the bicarbonate concentration at which the pulsed EPR measurements were carried out.

were first simulated in the time domain and then after introducing appropriate dead times (to simulate experimental conditions) were Fourier transformed to form frequency domain spectra. Because in our pulsed EPR experiments the excitation bandwidth of the pulses (10 G) was comparable to the line width of the ±1/2 transition, in simulations we assume that complexes in all orientations with respect to the magnetic field contribute equally to the calculated spectrum.

III. Results

Electrochemistry. The voltage−current curves corresponding to the electrochemical reduction of Mn$_{aq}^{2+}$ to Mn^0 in the voltammetry experiments are shown in Figure 1A. In each curve, the current reaches a maximum at a potential designated by E_p, the peak potential. For one- or two-electron reversible processes, the difference between the peak potential (E_p) and the midpoint potential ($E_{1/2}$) is equal to 28 mV and 14 mV, respectively.[30] In the discussion below, we use E_p (instead of $E_{1/2}$) for data plotting and analysis.

In the absence of added bicarbonate (curve 0 in Figure 1A), the peak potential, E_p, is observed at −1.200 V, which corresponds to a midpoint potential $E_{1/2} = -1.186$ V for the two-electron reduction of Mn^{2+} (Mn^{2+}/Mn^0 couple), in agreement with the literature values.[31] It is important to note that E_p does not depend on the concentration of Mn^{2+} (data not shown), although the height of the observed reduction wave is directly

5102 *J. Phys. Chem. B, Vol. 110, No. 10, 2006*

Dasgupta et al.

proportional to [Mn^{2+}] concentration (for [Mn^{2+}] = 55 μM to 1 mM). The difference between the potentials, the peak potential (E_p) and the midpoint potential ($E_{1/2}$), is equal to 30 mV. These facts indicate a diffusion-controlled and reversible transfer of two electrons. The cyclic voltage−current curves (0−13) do not show an anodic peak upon reversing the voltage sweep, indicating the irreversibility of the process. This irreversible behavior is typically observed for aqueous cations of metals that are weakly soluble or insoluble in mercury (Fe, Co, Ni, Mo, W, Mn).[32] At present, it is generally accepted that the cathodic reduction of Mn^{2+} ions on the mercury electrode is quasireversible and the absence of anodic peaks upon reversing the voltage sweep (Figure 1A, curve 0) results from dissolution of reduced Mn^0 within the mercury drop and the additional energy spent in forming of a manganese/mercury amalgam.[33,34] Thus, Mn^{2+} reduction at the Hg electrode can be expressed by the following two-step process

$$Mn^{2+}_{aq} + 2e^- \leftrightarrow Mn^0_{surface} \qquad (2)$$

$$Mn^0_{surface} \rightarrow Mn_{(Hg)} \qquad (3)$$
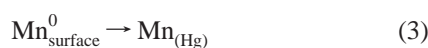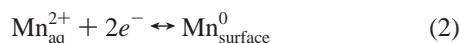
where the first reaction (eq 2) describes reversible reduction of the ion at the electrode surface, and the second reaction (eq 3) is irreversible dissolution of the metal to form an amalgam. The standard rate constant of an electrode process (k_S) for reduction of Mn^{2+} on a Hg electrode in 1 M NaClO$_4$ or NaCl is equal to 5×10^{-4} cm·s^{-1}, and the transfer coefficient, α, is equal to 0.66 at 30 °C. These values characterize the process of Mn^{2+} reduction as quasi- reversible according to Bond.[30] Therefore, despite the formal irreversibility of the reduction and reoxidation voltammograms, we can consider the reduction process as quasireversible and thus use standard equations to determine the stability constants and the stoichiometry of complexation.

In the presence of coordinating anions such as bicarbonate, Mn^{2+} may form a coordination complex with bicarbonate by displacing coordinated water molecule(s)

$$Mn^{2+} + qHCO_3^- \overset{K}{\rightleftharpoons} [Mn(HCO_3)_q]^{(2-q)} \qquad (4)$$
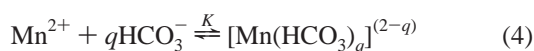
Here q defines the number of bicarbonate ions in the coordination shell of Mn^{2+}, and K is the stability constant of the complex (water ligands are not shown). Because bicarbonate is a negatively charged ligand, the formed complex [Mn(HCO$_3$)$_q$]$^{(2-q)}$ is expected to have a more negative reduction potential compared to Mn$^{2+}_{aq}$. Accordingly, we find that the peak potential in the Mn^{2+}−bicarbonate solutions shifts to more negative potentials at increasing bicarbonate concentrations (curves 4−13 in Figure 1A). Also, the peak current, I_p, decreases and the peak broadens because of complexation as more bicarbonate is titrated in solution. It is expected that complex formation affects only the reversible reduction step of eq 2, while not affecting the irreversible dissolution of Mn^0 shown in eq 3. In a simple case when Mn^{2+} speciation in bicarbonate solution is dominated by only one complex, for example, [Mn(HCO$_3$)$_q$]$^{(2-q)}$, the dependence of Mn^{2+} reduction potential (E_p) on bicarbonate concentration can be described by the Lingane equation[32]

$$E_p - E_p^{free} = -\frac{0.059}{n} \log K - q \frac{0.059}{n} \log[HCO_3^-] \qquad (5)$$

where potentials, E, are in volts, and $n = 2$ for two-electron reduction of Mn^{2+} to Mn^0. In this case, plotting the peak potential, E_p, versus the log of the bicarbonate concentration will result in a linear plot with a slope defining q and an intercept

TABLE 1: Mn^{2+} Stability Constants (K) with HCO$_3^-$/CO$_3^{2-}$ from the Electrochemistry and EPR Data at Room Temperature

Mn:HCO$_3^-$	literature data[19,34] K (μ)^a	this work K (μ)^a
1:1	63.1 M^{-1} (0)	22 $\pm$ 5 M^{-1} (0.1)
	18.6 M^{-1} (0.3)	18 $\pm$ 2 M^{-1} (0.3)
	2.82 M^{-1} (3)	
1:2	n.a	550 $\pm$ 200 M^{-2} (0.1)
		568 $\pm$ 50 M^{-2} (0.3)

^{a} μ: ionic strength of solution (in M).

defining K. E_p^{free} designates the peak potential corresponding to the Mn^{2+} aqua ion.

The dependence of E_p on bicarbonate concentration is shown in Figure 1B where three distinct regions of bicarbonate concentrations can be distinguished by their different slopes. Assuming that the Lingane approximation is applicable (i.e., the slope of each linear region corresponds to one dominant [Mn(HCO$_3$)$_q$]$^{(2-q)}$ species), the following three species can be deduced. At low bicarbonate concentrations (0−10 mM), the Mn^{2+} peak potential is insensitive to added bicarbonate ($q = 0$), which reveals that the free Mn$^{2+}_{aq}$ ion is the dominant species in solution. At the highest bicarbonate concentrations (50−200 mM), a linear phase of the potential yields a slope of 60 mV/log [HCO$_3^-$], corresponding to $q \cong 2$ at $n = 2$. Thus, [Mn(HCO$_3$)$_2$] is the most abundant species at these high concentrations. Extrapolation of the fitted line to log[HCO$_3^-$] = 0 allows evaluation of the standard reduction potential, $E°$ = −1.275 V, and the stability constant, $K_2 = 349$ M^{-2} (at 22 °C), for this species.

At intermediate bicarbonate concentrations (10−60 mM), a slope of 14 mV/log[HCO$_3^-$] is observed, which formally corresponds to $q = 0.5$ and thus indicates a complex consisting of two Mn^{2+} per one HCO$_3^-$, that is, [Mn$_2$(HCO$_3$)]$^{3+}$. This stoichiometry is unreasonable in the context of the Lingane equation because it deals only with complexes where q is an integer and ≥ 1.[35] To verify whether dimeric Mn$_2$ clusters occur in solution, as suggested by the slope $q = 0.5$, we examined the dependence of E_p on Mn^{2+} concentration between 55 μM and 1 mM. The results show that E_p does not depend on the Mn^{2+} concentration. Also, the reduction current, I_p, depends linearly on [Mn^{2+}], which clearly shows that the stoichiometry of 2:1 is not feasible (Figure S1 in the Supporting Information). Additional support for the absence of dimeric Mn^{2+} clusters in solution speciation is provided below by analyzing the EPR data. We conclude that the slope with $q = 0.5$ is an artifact of the use of the Lingane equation and its underlying assumptions of nonoverlapping speciation.[35]

The titration data were therefore reexamined using the DeFord−Hume method (eq 6), which explicitly accounts for two or more species present in solution at equal or substantial fractions.[35] The DeFord−Hume equation

$$E_p - E_p^{free} = -\frac{0.059}{n} \log(1 + \sum_q K_i * L^i) \qquad (6)$$

where K_i denotes the stability constant for each complex involved in speciation, was used to fit the data (shown with a dashed curve in Figure 1B). The fit is equally good as the Lingane equation although the new model shown in eq 7 does not involve any dimeric Mn$_2$ complexes and only involves monomeric Mn^{2+} species in solution. The stability constants derived from the fit are shown in Table 1, together with other
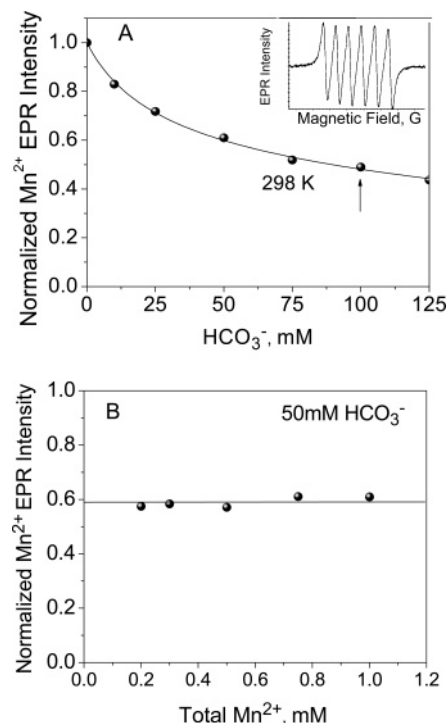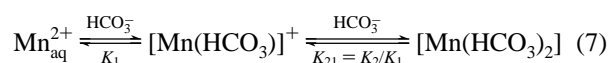
Figure 2. (A) Dependence of the Mn^{2+} EPR signal intensity on bicarbonate concentration in aqueous solution at room temperature (Mn^{2+} concentration 0.5 mM, pH 8.3). Fit to an equilibrium model described in eq 8 is shown with a solid line. The inset shows typical Mn^{2+} EPR signal in aqueous solution centered at g 2.0. (B) Dependence of the Mn^{2+} EPR signal intensity (normalized to total amount of Mn^{2+} in the sample) as a function of Mn^{2+} concentration at fixed 50 mM NaHCO$_3$ in aqueous solution at room temperature. The straight line shows the invariance on Mn^{2+} concentration, clearly eliminating the presence of any Mn^{2+} clusters in speciation.

data available from the literature and obtained through other techniques.[36]

$$\text{Mn}^{2+}_{aq} \underset{K_1}{\overset{\text{HCO}_3^-}{\rightleftharpoons}} [\text{Mn(HCO}_3)]^+ \underset{K_{21}=K_2/K_1}{\overset{\text{HCO}_3^-}{\rightleftharpoons}} [\text{Mn(HCO}_3)_2] \quad (7)$$

The stability constant, K_2, of the 1:2 complex Mn(HCO$_3$)$_2$ can be viewed as a product $K_2 = K_1K_{21}$, which involves two reversible steps, that is, binding of the first (K_1) and the second (K_{21}) bicarbonate ligands. The binding constant of the second bicarbonate ligand can then be estimated as $K_{21} = K_2/K_1 = 568/18.5 = 30.7$ M^{-1}. The fact that K_{21} and K_1 are comparable makes it evident that at intermediate bicarbonate concentrations (10–60 mM in Figure 1B) two complexes with stoichiometries 1:1 and 1:2 are present at comparable fractions in solution. The Lingane equation (eq 5) is clearly not applicable in this situation, and the misleading slope $q = 0.5$ results from the transient region where more than two distinct Mn^{2+} species are present in the equilibrium. This analysis serves as a caveat for using the Lingane equation when interpreting changes of redox potentials in metal−ligand solution equilibria.

EPR Spectroscopy. *Room-Temperature EPR Measurements.* In liquid solutions, Mn^{2+} is subject to fast rotational and tumbling motion, which causes all anisotropic interactions in the spin-Hamiltonian (eq 1) to average out, resulting in an EPR spectrum (shown as the inset in Figure 2A), which can be described by only using isotropic interactions. The spectrum consists of six lines centered at $g = 2.0$, which are split by isotropic hyperfine coupling with the ^{55}Mn nucleus ($I = 5/2$). Each of the six hyperfine lines consists of five overlapping electron spin transitions within the $S = 5/2$ electron spin

multiplet of Mn^{2+}. These five transitions occur between adjacent M_S sublevels ($M_S = \pm5/2, \pm3/2, \pm1/2$, where M_S is the electron spin projection) and are weighted by the respective transition probabilities, $S(S + 1) - M_S(M_S + 1)$, to contribute nonequally to the EPR signal intensity.[37] In addition, incomplete motional averaging of the anisotropic interactions (like ZFS and anisotropic hyperfine interactions) can result in M_S-dependent broadening of the transitions, and thus those transitions that involve higher M_S states are usually broader than transition between the inner states $M_S = +1/2$ and $-1/2$.[38] This nonequivalent broadening results in additional weighting of the transitions so that broader transitions (higher M_S) contribute smaller peak intensity into the EPR signal.

The Mn^{2+} aqua ion has small but finite ZFS ($\sim$280−300 MHz) arising from small distortions to the octahedral symmetry of the six water ligands.[22] Complex formation with bicarbonate further reduces the symmetry of the ligand field around the Mn^{2+} ion and thereby causes the ZFS to increase. A larger ZFS in the complex results in broader electron spin transitions and thus a weaker intensity of the six-line EPR signal compared to more symmetric Mn$^{2+}_{aq}$ ion. The transitions that involve higher spin states $M_S = \pm3/2$ and $\pm5/2$ are mostly affected and can be broadened to contribute little or no intensity in the six-line EPR signal. However, the inner spin transition between $M_S = +1/2$ and $-1/2$ (which contributes approximately 25% of the total signal intensity) is least affected and broadened only to the second order by ZFS. Thus, the lower symmetry Mn^{2+}−bicarbonate complexes might be expected to show fewer than 25% of the EPR intensity of the more symmetric Mn$^{2+}_{aq}$ ion based on transition probabilities.

Upon addition of anions such as bicarbonate, three Mn^{2+} complexes of different ligand field symmetries coexist in solution as represented by eq 7. If these complexes are assumed to be in slow exchange equilibrium (10^{-7} to 10^{-8} s),[39] then the EPR spectrum at any concentration of bicarbonate can be represented as a weighted sum of the individual Mn^{2+} signals from each involved complex. At small bicarbonate concentrations, the Mn$^{2+}_{aq}$ ion prevails in solution and therefore the EPR intensity is expected to be high. With increasing bicarbonate concentration, the low-symmetry Mn^{2+}−bicarbonate complexes become abundant in solution and thus the EPR signal reduces in intensity.

Figure 2A describes the experimentally observed changes in the intensity of the six-line Mn^{2+} EPR spectrum (normalized to the intensity of Mn$^{2+}_{aq}$ signal) as a function of bicarbonate concentration. Because the line width of the hyperfine lines in the spectrum remains invariant with ligand concentration, the peak-to-peak intensity was used to plot the spectral intensity. The normalized intensity decreases at higher bicarbonate concentrations, indicating that the equilibrium shifts from the free Mn$^{2+}_{aq}$ toward the lower symmetry bicarbonate complex(es). The drop of intensity approaches saturation at about 30−40% of the initial Mn^{2+} intensity: This residual intensity corresponds to the lower symmetry complex(es) whose intensity comes primarily from the $\pm1/2$ transition, as discussed earlier. The experimental points were fitted using a model shown in eq 8

$$I(c) = \sum_{i=0}^{2} n_i(c) \cdot I_i \quad (8)$$

where $n_i(c)$ and I_i are the concentration-dependent statistical weights and individual spectral intensities, respectively, of the Mn^{2+} complexes with i bicarbonate ligands; $n_i(c)$ was calculated

using the equilibrium model (eq 7) and assuming the equilibrium constants, K_i, to be close to those derived from the electrochemical titration data (Figure 1B). The good fits (the dashed line in Figure 2A) were obtained at $K_1 = 22 \pm 5$ M^{-1} and $K_2 = 550 \pm 200$ M^{-2} and the intrinsic intensity coefficients $I_1 = 0.3 \pm 0.1$ and $I_2 = 0.45 \pm 0.15$ for complexes with one and two bicarbonate ligands, respectively, (the spectral intensity, I_0, of the Mn$_{aq}^{2+}$ ion was assumed to be unity). The derived values for I_1 and I_2 are consistent with the expected lower symmetry of the ligand field in the Mn^{2+}−bicarbonate complexes (and thus larger ZFS and lower EPR intensity) as compared to Mn$_{aq}^{2+}$. The fact that $I_1 < I_2$ indicates that symmetry of the ligand field is higher in the case of two bicarbonate ligands bound to Mn^{2+}.

To test for the presence of cluster-like species in solution (i.e., Mn^{2+} dimer as might be inferred from the slope $q = 0.5$ in the electrochemistry titration data), we examined the EPR intensity at a fixed bicarbonate concentration (50 mM) and over the 0.2−1 mM range of Mn^{2+} concentrations, as shown in Figure 2B. The observed zero-order dependence of the fractional Mn^{2+} intensity (i.e., weighted by the total amount of Mn^{2+} in solution) as seen in Figure 2B rules out the possibility of oligomeric forms of Mn^{2+} in solution speciation.

Frozen-Solution EPR Measurements. The perpendicular-mode EPR spectra on Mn^{2+} in 25% CH$_3$OH/water frozen glass at 8−77 K shows a characteristic six-line signal centered around $g = 2$ and a low intensity feature at $g = 4$ (Figure S2A in the Supporting Information). The signal at $g = 2$ arises from monomeric Mn^{2+} complexes. Its peak-to-trough intensity when plotted as a function of bicarbonate concentration (Figure S3 in the Supporting Information) can be used to evaluate the stability constants of [Mn(HCO$_3$)$^+$] and [Mn(HCO$_3$)$_2$] complexes formed in solution, in a fashion similar to that described above for the room-temperature EPR data. The stability constants derived from the fit in frozen solutions are similar to those extracted from the room-temperature experiments. This agreement indicates that there are no appreciable changes in Mn^{2+}−bicarbonate speciation equilibrium upon addition of 25% methanol and/or upon freezing to low temperatures.

Also extracted from the fit are individual spectral intensities (I_i) of the contributing complexes. The values $I_1 = 0.15 \pm 0.05$ and $I_2 = 0.38 \pm 0.1$ in frozen solution are lower as compared to the room-temperature results. This difference is not unexpected because there is no motional averaging at frozen solution and thus the transitions with higher M_S are broadened more significantly by ZFS and therefore contribute smaller intensity than those at room temperature.

The weak $g = 4$ signal observable in the EPR spectra at low temperatures is assignable to either a double-quantum transition of monomeric Mn^{2+} or to a transition within the excited state $S = 1$ of an antiferromagnetically coupled dimanganese complex Mn^{2+}−L−Mn^{2+}.[40] To resolve this uncertainty, the intensity of the $g = 4$ signal was examined while varying the Mn^{2+} concentration (Figure S2B in the Supporting Information). The intensity is found to scale linearly with Mn^{2+} concentration, proving that the $g = 4$ feature belongs to a monomeric form(s) of Mn^{2+}. This assignment is in line with the room-temperature EPR and electrochemistry data showing that the "dimer"-like species (or oligomeric Mn^{2+}) are absent in the bicarbonate solutions.

Field-Sweep Pulsed EPR Spectra. All of the pulsed EPR experiments reported below were done on samples with 0.5 mM Mn^{2+} and with no added or 100 mM bicarbonate in solution. As can be estimated using the equilibrium constants in Table
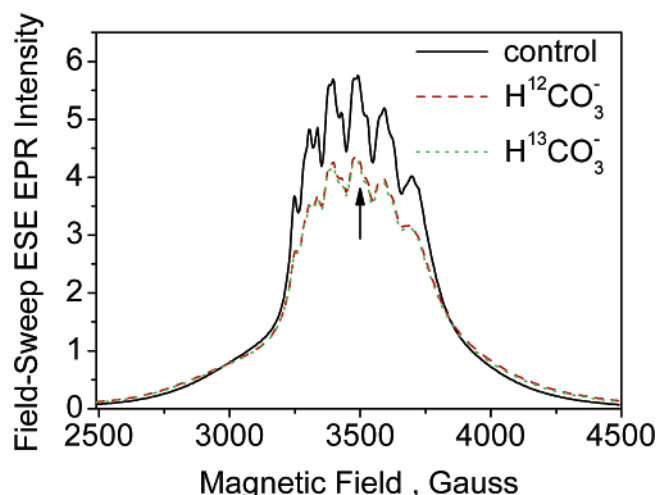

Figure 3. EPR absorption signal of Mn^{2+} (0.5 mM) detected using the two-pulse ESE field-sweep technique in frozen glass solution (H$_2$O/CH$_3$OH) at 10 K: (solid black) with no added bicarbonate; (dashed red) with 100 mM NaH^{12}CO$_3$; (dashed green) with 100 mM NaH^{13}CO$_3$. The vertical line indicates the magnetic field position (3490 G) at which ESEEM, ENDOR, and HYSCORE measurements were carried out. Interpulse delay $\tau = 400$ ns was used in the field-sweep experiments.

1, at 100 mM bicarbonate the total Mn^{2+} in solution is represented by a mixture of 70% [Mn(HCO$_3$)$_2$], about 20% [Mn(HCO$_3$)]$^+$, and 10% Mn$_{aq}^{2+}$.

Figure 3 shows the absorption EPR line shapes of Mn^{2+} in the absence and presence of added bicarbonate, recorded using field-sweep electron spin echo (ESE)-detected EPR. In addition to the resolved six-line hyperfine pattern at the center of the spectrum (also observed in the first-derivative CW EPR spectra, Figure S2A in the Supporting Information), the absorption line shapes in Figure 3 also reveal a broad underlying signal that extends for hundreds of gauss on either side of the central $g = 2$ feature. A detailed interpretation of the Mn^{2+} absorption spectrum, in the case of the Mn^{2+} aqua ion, has been given elsewhere.[22] It was shown that the Mn^{2+} spin-Hamiltonian (eq 1), involving two isotropic terms (electron Zeeman and ^{55}Mn hyperfine interactions) and one anisotropic ZFS coupling, is sufficient to fully describe the absorption spectrum. Nonzero ZFS (estimated as $D = 280-300$ MHz for Mn$_{aq}^{2+}$)[22] both broadens and shifts four out of five electron spin transitions, $\pm 1/2 \leftrightarrow \pm 3/2$ and $\pm 3/2 \leftrightarrow \pm 5/2$, away from $g = 2$ and thus spreads them around the center to produce the broad signal. The central transition, $+1/2 \leftrightarrow -1/2$, is only susceptible to the second-order broadening by ZFS and forms the resolved six-line hyperfine pattern that sits on top of the broad signal. Additional broadening effects come from significant D and A strains (caused by heterogeneity in the ligand field) that affect the outer transitions to a larger extent than the inner transitions.[22]

Upon addition of 100 mM bicarbonate, the absorption EPR spectrum transforms to show less intensity at the center and stronger intensity at the spectrum wings (Figure 3). This spectral transformation is expected for [Mn(HCO$_3$)$_2$], which has a lower ligand field symmetry and a larger ZFS as compared to Mn$_{aq}^{2+}$. The larger ZFS forces the outer transitions, $\pm 1/2 \leftrightarrow \pm 3/2$ and $\pm 3/2 \leftrightarrow \pm 5/2$, to spread further around the spectrum center, and thus to produce even broader underlying signal and an increased intensity at the spectral wings. In addition, the increased ZFS causes a second-order broadening of the inner transition ($+1/2 \leftrightarrow -1/2$), resulting in lower signal intensity at the center. This spectral transformation can be qualitatively reproduced in spectral simulations using $D \approx 700$ MHz.
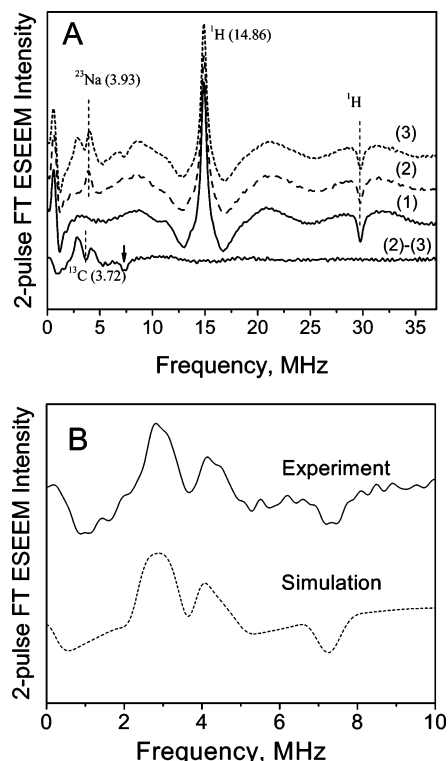
Mn^{2+} Speciation in Aqueous Solutions of Carbonate

J. Phys. Chem. B, Vol. 110, No. 10, 2006 **5105**

Figure 4. (A) Cosine FT traces of the two-pulse ESEEM of Mn^{2+} (0.5 mM) in frozen glass solution (H$_2$O/CH$_3$OH) recorded at 3490 G and 10 K. Trace 1, no added bicarbonate; trace 2, 100 mM NaH^{12}CO$_3$; and trace 3, 100 mM NaH^{13}CO$_3$. Trace 2−3 at the bottom is the difference spectrum of 2 and 3 and shows the nuclear spin transitions arising only from ^{13}C nuclei (this difference spectrum is also shown in B). The vertical lines show the positions of Zeeman frequencies for ^{1}H, ^{23}Na, and ^{13}C nuclei at 3490 G. The arrow indicates the sum combination line of ^{13}C. (B) Comparison of experimental (solid line) and simulated (dash−dot line) ^{13}C ESEEM spectra. Simulation parameters are shown in Table 2.

However, we have not attempted a detailed spectral simulation owing to spectral complexity associated with the presence of a background signal from 20% Mn(HCO$_3$)$^+$ and a lack of exact knowledge of spin relaxation times (T_2 and its orientation dependence), which are essential for accurate simulation of the ESE-detected spectra. Finally, we note that the Mn^{2+} spectral transformation is identical upon addition of ^{12}C or ^{13}C bicarbonate. This lack of resolution is expected because the ligand ^{13}C hyperfine couplings are small and therefore unresolved in the broad EPR line width. ESEEM/ENDOR methods are applied to resolve this small coupling, as described below.

^{13}C Hyperfine Coupling for Bicarbonate Ligands. Two-pulse ESEEM spectra were recorded at magnetic field 3490 G (marked by an arrow in Figure 3), the center of one of the resolved ^{55}Mn hyperfine lines. This field corresponds mostly to the $+1/2 \leftrightarrow -1/2$ transition; however, the other four transitions also contribute appreciably (about 30−40% of the spectral intensity) at this field. The cosine FT ESEEM traces recorded for Mn^{2+} frozen solutions in the absence and presence of ^{12}C or ^{13}C bicarbonate are shown in Figure 4A. In the absence of bicarbonate, only two peaks are seen in the spectrum: a positive peak at proton Zeeman frequency 14.96 MHz (ν_H) and a negative peak at 29.8 MHz ($\sim 2\nu_H$). These peaks, also known as the matrix lines, arise from weakly coupled ^{1}H nuclei surrounding the Mn^{2+} aqua ion.[41] The low-frequency feature at around $\sim$0.5 MHz is an artifact of the FT procedure.

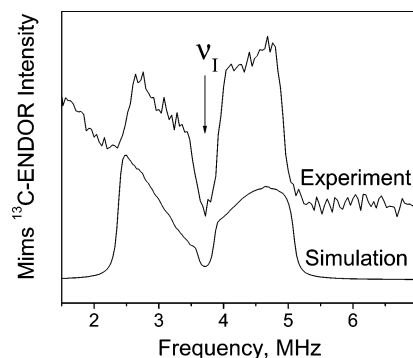Upon addition of ^{12}C ($I = 0$) bicarbonate (NaHCO$_3$), the spectrum (trace 2 in Figure 4A) shows the new peak at 3.93

Figure 5. Experimental (top trace) and simulated (bottom trace) Mims ^{13}C ENDOR spectra of Mn^{2+} (0.5 mM) in frozen glass solution (H$_2$O/CH$_3$OH) at 3490 G and 10 K. The experimental spectrum was obtained by subtraction of the spectra recorded using ^{13}C- and ^{12}C-labeled bicarbonate. The vertical arrow labeled ν_I indicates the position of ^{13}C Zeeman frequency at 3490 G. Simulation parameters are given in Table 2.

MHz, which is assigned to the matrix frequency of ^{23}Na ($I = 3/2$). Upon addition of ^{13}C ($I = 1/2$) bicarbonate (NaH^{13}CO$_3$), the spectrum (trace 3) shows additional lines in the spectral region of 2−5 MHz, overlapping with the ^{23}Na line. These additional features can be revealed clearly by subtracting the normalized spectra of ^{13}C and ^{12}C bicarbonate that eliminates the lines from ^{1}H and ^{23}Na nuclei (bottom trace in Figure 4A and also zoomed in Figure 4B). The prominent features in this difference spectrum are the two positive-amplitude peaks at 2.9 and 4.26 MHz and also their sum combination at 7.34 MHz, which has negative amplitude. The two positive peaks are positioned around the Zeeman frequency of ^{13}C ($\nu_I = 3.72$ MHz at 3490 G) and correspond to ^{13}C nuclear transition frequencies within two electron spin manifolds $M_S = \pm 1/2$.[55] Their splitting of 1.4 MHz gives an approximate measure of isotropic part (a_{iso}) of the ^{13}C hyperfine coupling. The individual line width of each line, $\sim$1 MHz, gives a measure of anisotropic part (T) of the ^{13}C hyperfine coupling.[29] The significant values of a_{iso} and T indicate that this ^{13}C belongs to a bicarbonate ligand in the first coordination shell of Mn^{2+}.

The sum combination line at 7.34 MHz is downshifted from the value $2\nu_I$ (7.44 MHz), the double Zeeman frequency of ^{13}C at 3490 G. It has been shown that the combination line can shift from $2\nu_I$ to higher or lower frequencies depending on the magnitude and relative signs of the dipolar part (T) of the ^{13}C hyperfine tensor and the axial ZFS parameter (D), and also on the relative orientation of these two tensors.[29] The negative shift in our case indicates either the same sign of T and D at 0° orientation of the two tensors or their opposite sign at 90° orientation. Although the shift of the combination line can be useful in estimating T and D, more accurate values can be extracted from the correlation 2D HYSCORE spectra (see below).

Mims ENDOR was recorded at 3490 G, and the difference spectrum (^{13}C bicarbonate − ^{12}C bicarbonate) is shown in Figure 5 in the region around ^{13}C Zeeman frequency (see Figure S5 in the Supporting Information for the experimental raw data). The two broad lines at 3.0 and 4.2 MHz are the same as those seen in the ESEEM spectrum; however, their anisotropic line shapes are much better resolved in the ENDOR spectrum. These anisotropic line shapes arise from the orientation dependence of the ^{13}C nuclear transition frequencies in the Mn^{2+} complex. At 3490 G, many Mn^{2+} complexes with different orientations are excited by microwave pulses and their weighted contributions sum up to produce the broad anisotropic lines. Each line
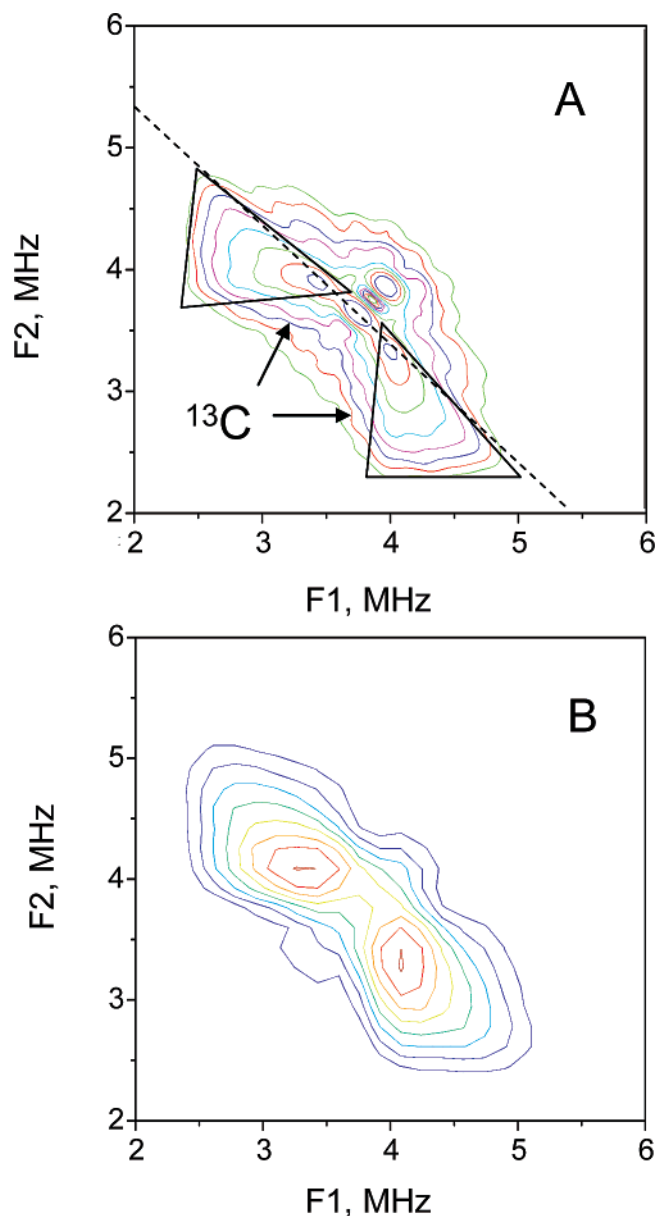
Figure 6. (A) Contour plots of experimental (A) and simulated (B) 2D HYSCORE spectra (shown in the range of 2−6 MHz) of Mn^{2+} in frozen solution (H_2O/CH_3OH) in the presence of 100 mM $NaH^{13}CO_3$, recorded at 3490 G and 10 K. The position of the ^{13}C cross peaks are outlined by triangles for clarity. Matrix lines from distant ^{13}C and ^{23}Na nuclei are also seen at (3.72, 3.72) MHz and (3.92, 3.92) MHz. The dashed line is shown perpendicular to the main diagonal of the 2D spectrum and passing through (ν_I, ν_I). The entire body of the ^{13}C cross peaks is positioned below this line. Simulation is done using parameters from Table 2.

shows two turning points corresponding to minimum and maximum nuclear transition frequencies in their orientation dependence. These turning points are useful for accurate determination of the ^{13}C hyperfine parameters in spectral simulations.

Two-dimensional (2D) HYSCORE was done at 3490 G in order to correlate the ^{13}C nuclear transition frequencies in the two $M_S = \pm 1/2$ sublevels. Figure 6A shows the contour plot of the 2D spectrum in the low-frequency region where lines from ^{13}C are expected. Only the (+ +) quadrant of the full 2D spectrum is shown because the other (+ -) quadrant shows no additional features. The peaks lying along the main diagonal of the 2D spectrum correspond to the matrix lines of weakly

coupled ^{13}C and ^{23}Na. The two off-diagonal cross peaks are also seen and correlate the ^{13}C nuclear transitions in the two electron spin sublevels. These two cross peaks are mirror images of each other with respect to the main diagonal of the 2D spectrum. Each cross peak has a pyramidal shape with a triangular base that is outlined for clarity in Figure 6A. The edges of the triangular base, although not resolved clearly, can be outlined qualitatively from analyzing the cross-peak slices along the x and y directions in the 2D plot (e.g., some slices are seen in a 3D surface plot presentation of this spectrum in Figure S7 in the Supporting Information and show a rectangular line shape with clearly resolved low- and high-frequency turning points). The top of the pyramid is shifted toward one corner of the triangular base and peaks at 2D coordinates (3.45, 4.05) MHz.

These pyramidal cross-peak shapes arise from superposition of many orientations of the Mn^{2+} complex in frozen solution samples and result from orientation-dependent correlation of the ^{13}C nuclear transition frequencies in two electron spin manifolds $M_S = \pm 1/2$. The triangular cross-peak shape indicates that the spin-Hamiltonian of Mn^{2+} has rhombic symmetry that can arise either from rhombicity in ^{13}C hyperfine or ZFS tensor or (in case of axial tensors) from noncollinear orientation of the two tensors.[42] The corners of the triangular base represent three turning points in the anisotropic cross-peak line shape. This feature contrasts with only two turning points found in the spectral line shapes of the 1D ENDOR spectrum in Figure 4. However, when the 2D spectrum in Figure 6A is projected onto the horizontal (or vertical) axis, two of the three turning points coincide, resulting in a line shape with only two turning points, consistent with the 1D ENDOR spectrum. We also point out that the triangular cross peaks are shifted below the line (shown dashed in Figure 6A) that is perpendicular to the main diagonal and passes through coordinates (ν_I, ν_I) in the 2D spectrum. This shift to lower frequencies has the same origin as the negative shift of the sum combination line observed in the 1D ESEEM spectrum (Figure 4) and it can only arise for specific values of T and D and at specific orientations of the two tensors.

Simulations of the 2D HYSCORE spectrum were performed to extract the ZFS coupling and the ^{13}C hyperfine parameters associated with the Mn−bicarbonate complexes. Because our goal was to reproduce the line shapes of the cross peaks and not their relative intensities, only the inner transition ($-1/2 \leftrightarrow +1/2$) was taken into account for the HYSCORE simulations. The extracted parameters from HYSCORE simulations were then refined in simulations of 1D ESEEM and ENDOR spectra. In this HYSCORE simulation our criteria for the best fit were (1) the pyramidal shape of the ^{13}C cross peak with a triangular base and three turning points, (2) the peak intensity of the cross peak that is shifted toward one (inner) corner of the triangular base, (3) the entire body of the cross peak shifted to low frequencies, that is, below the dashed line in Figure 6A. This set of constraints allowed us to uniquely determine the simulation parameters as explained below.

Six fitting parameters were involved in the simulation: the isotropic (a_{iso}) and anisotropic (T) components of the ^{13}C hyperfine tensor (axial symmetry of the tensor was assumed), the coupling (D) and rhombicity (E) of the ZFS tensor, and two Euler angles (β and γ) to define orientation of the hyperfine tensor in the ZFS tensor frame (only two Euler rotations are needed because we assumed the hyperfine tensor to be axial). The Euler angles, β and γ, are defined as two subsequent rotations of the hyperfine tensor eigen-frame around X and then

TABLE 2: Spin-Hamiltonian Parameters for the 1:2 Complex, $Mn^{2+}(CO_3^{2-})(HCO_3^-)(OH_2)_3$, as Derived from the 2D HYSCORE Simulations

a_{iso} (MHz)	T (MHz)	D (MHz)	E (MHz)	Euler angles (β, γ) in degrees
−1.1 (±0.1)	0.8 (±0.1)	−700 (±50)	±115 (±25)	90 (±10)
				90 (±45)

Z axes in the eigen-frame of the ZFS tensor. The initial settings for three out of six parameters were estimated from the above analysis of the ESEEM/ENDOR spectra (e.g., $a_{iso} = 1.4$ MHz and $T = 1$ MHz) and from the qualitative simulations of the absorption EPR spectrum (e.g., $D \approx 700$ MHz). The remaining parameters (E, β, and γ) were allowed to span over all possible values. The simulated HYSCORE spectrum was highly sensitive to the relative signs of D and T and also to angle β between the principal axes of the two tensors (e.g., see some selected simulations for different values of D and β in Figure S6 in the Supporting Information). Therefore, these three parameters were optimized first. Considering the case of T and D having the same sign, only the narrow range of β from 0 to 10 degrees produced the triangular cross-peak shapes positioned below the dashed diagonal line in Figure 6A (which thus satisfies criteria 1 and 3). However, the peak intensity was shifted to the centroid of the triangular shape, unlike in the experimental spectrum where the peak intensity is at the corner of the triangular base (criteria 2). When β was increased close to 45°, the triangular shape shrinked to stripes with no sharp edges positioned along the dashed line in Figure 6A, and for $\beta > 45°$ the cross peaks were positioned above this line. Thus, fixing the signs of T and D to be the same and at any angle β is insufficient to simulate the experimental spectrum.

Considering unlike signs of T and D, angles β from 0 to 45° resulted in cross peaks above the dashed line, while $45 < \beta \leq 70°$ produced the "bell"-shaped peaks (Figure S6C in the Supporting Information). However, for values $70 < \beta \leq 90°$, the cross peaks are triangular-shaped and below the dashed line. Also at β close to 90°, the peak intensity of the cross-peak shifts to the inner corner of the triangular base as is observed in the experimental spectrum (Figure S6E in the Supporting Information). Thus, all three fitting criteria are satisfied for T and D of opposite signs and $\beta = 90 \pm 10°$. Fine-tuning of the simulated spectrum was performed next by varying γ, E, and a_{iso}. We found that introducing a nonzero E sharpened the turning points of the triangular-shaped cross peak, making it closer to the experimental line shape. The closest fit was obtained at $D/6 < E < D/3$ and angles $45 < \gamma \leq 90°$. In the final step, the accurate position of the peaks was adjusted by varying a_{iso} in the 1.0–1.3 MHz range. The best-fit parameters are summarized in Table 2.

The best-fit parameters obtained from HYSCORE simulations were then used to simulate the 1D ESEEM and ENDOR spectra, and an excellent agreement was found between the simulated and experimental spectra as demonstrated in Figures 4 and 5. Both line shapes and line positions, including two line-shape turning points, are reproduced in the simulated spectra. To obtain the correct relative intensities of the ^{13}C transitions in the simulated ESEEM spectrum, it was important for us to include the contributions from electron spin transitions that involve higher M_S states. Assuming 70–80% of the ESEEM intensity from the $+1/2 \leftrightarrow -1/2$ transition and the other 20–30% from other transitions produces the best fit to the experimental intensities as shown in Figure 4B (the simulations with other

fractional contribution from the high spin state transitions are shown for comparison in Figure S4B in the Supporting Information).

To deduce the absolute number of ^{13}C nuclei bound to Mn^{2+}, we compared the absolute peak intensities in the normalized simulated ESEEM spectra to the experimental ESEEM (Figure S4A in the Supporting Information). The ESEEM simulations for two equivalent ^{13}C nuclei were done using an approximation of "uncorrelated orientations of the nuclei"[43] and accordingly the time domain for two nuclei was calculated as a simple square of the time domain of a single ^{13}C. The validity of this approximation was examined by extending the simulations to account for specific relative orientations of the two ^{13}C nuclei in the complex. It was found that for any orientation of the two nuclei (including the special case of "trans" orientation of the ligands where suppression of modulation depth is observed in $S = 1/2$ and $I = 1/2$ systems[44]) yielded closely comparable results to the approximation of "uncorrelated orientations". By comparing the simulations for one and two nuclei, it was concluded that only one ^{13}C nucleus contributes to the observed experimental ESEEM spectra (see Figure S4A). The second ^{13}C of the second bicarbonate ligand in $[Mn(HCO_3)_2]$ is probably coordinated in a different mode; therefore, it has a different hyperfine coupling and is not observed in the ESEEM spectra.

Hyperfine Interactions to Mn^{2+} Ligand Protons. Mims ^1H ENDOR was used to probe the hyperfine couplings to ligand protons in the coordination sphere of Mn^{2+}. The spectra recorded at three different concentrations of added bicarbonate in solution are shown in Figure 7A. All three spectra are quite similar and show the same set of resolved peaks (labeled with arrows) with only their relative intensities varying with bicarbonate concentration. The most intense peak at 14.9 MHz (labeled as ν_p) and also the small features that are partially resolved on this peak correspond to interactions to remote protons from the 2nd and farther coordination shells of Mn^{2+}. All other resolved peaks are due to protons of the water ligands from the 1st coordination sphere of Mn^{2+} (labeled with ±1/2 and ±3/2) and correspond to nuclear spin transitions from the complexes orientated perpendicular to the static magnetic field arising from the electron spin manifolds $M_S = \pm1/2$ and $\pm3/2$, respectively.[22] As reported previously by Tan et al.[22] and Manikandan et al.,[45] there are additional overlapping features that arise from the parallel orientations of the complex that are hidden underneath the more pronounced perpendicular features (e.g., weak parallel features from the $M_S = \pm1/2$ sublevels overlap with the perpendicular features from the $M_S = \pm3/2$ sublevel).

Upon addition of bicarbonate, no new peaks appear in the ENDOR spectra. At 100 mM bicarbonate, 80% of Mn^{2+} has two bicarbonate ligands but no new peaks assignable to bicarbonate protons could be resolved. Protons of the bicarbonate ligands are probably weakly coupled to the Mn^{2+} ion (because of the longer proton−Mn^{2+} distance) and their transitions must be hidden unresolved in the intense matrix ^1H line. We also notice that the resolved peaks from the water ligands (labeled with ±1/2 and ±3/2 in Figure 7) do not change their position and shape but only their intensity decreases upon addition of bicarbonate and formation of the Mn^{2+}−bicarbonate complex. The peaks become less intense as a greater fraction of the complexes form at higher bicarbonate concentrations. This suggests that bicarbonate ligands bind to Mn^{2+} by replacing some of the water ligands (therefore the decrease in the intensity of the peaks), but the coordination geometry of the remaining water ligands is not affected (therefore the peak frequencies are unchanged).
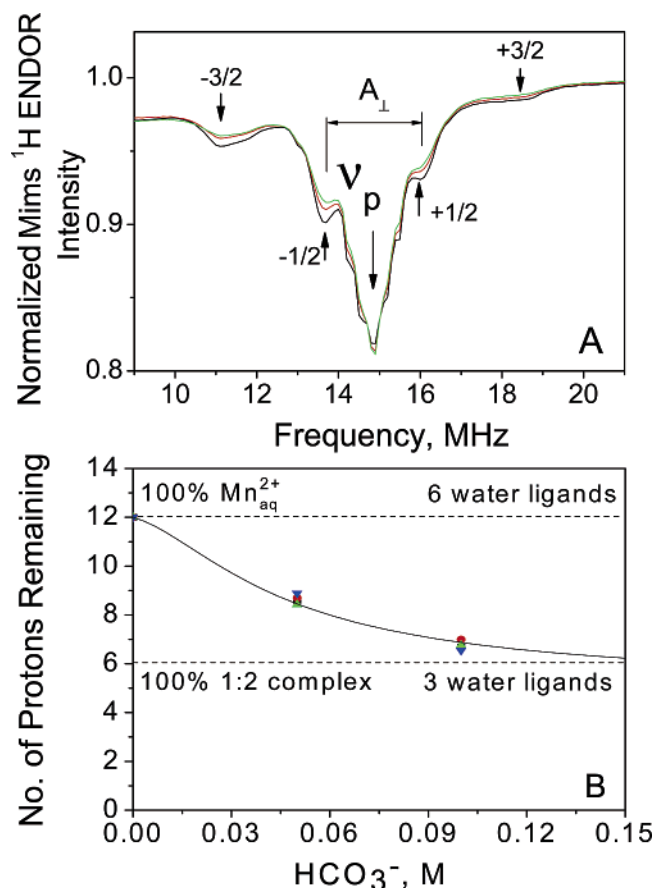
Figure 7. (A) Mims ¹H ENDOR spectra of Mn²⁺ (0.5 mM) in frozen glass solution (H₂O/CH₃OH) at 3490 G and 10 K, and at different concentrations of added NaHCO₃: (black) 0 mM, (red) 50 mM, and (green) 100 mM. The ¹H matrix line is shown by the arrow marked by ν_p. The lines marked with ±1/2 (perpendicular feature) and ±3/2 (perpendicular feature, although a small contribution from the ±1/2 parallel feature is also present) are from protons of water ligands and arise from electron spin manifolds ±1/2 and ±3/2, respectively. Their splitting gives a measure of the perpendicular component of ¹H hyperfine coupling (A⊥). Each ENDOR spectrum was normalized to the respective echo intensity in the absence of RF pulse. (B) Normalized intensities of the ¹H ENDOR lines from A are plotted as a function of bicarbonate concentration. These lines are from the water ligands to Mn²⁺ and correspond to the four electron spin sublevels: $M_S = -3/2$ (●), −1/2 (■), +1/2 (▲), and +3/2 (▼). The line intensities of each of the transitions were normalized by the respective line intensities in the Mn²⁺$_{aq}$ spectra (no added bicarbonate) and 12 protons were assumed in the first coordination shell of Mn²⁺$_{aq}$. The upper and lower horizontal dashed lines mark the normalized ENDOR intensities for Mn²⁺$_{aq}$ and for the 1:2 complex, [Mn(CO₃)(HCO₃)(H₂O)₃]⁻, respectively. The solid line represents the fit to the model shown in eq 9.

Reduction of the peak intensity of the $M_S = \pm 1/2$ and $\pm 3/2$ transitions as a function of added bicarbonate can be used to assess the number of remaining water ligands in the coordination shell of the Mn²⁺ complexes. Figure 7B shows the normalized intensity of the ENDOR peaks plotted as a function of added bicarbonate. Because the $M_S = \pm 1/2$ transitions overlap with the matrix line (ν_P), their intensities were determined as peak-to-trough amplitudes in the first derivative plots (calculated numerically) of the ENDOR spectra. This approach enables the extraction of accurate intensities of these transitions without requiring spectral deconvolution. The peak intensities for the $\pm 3/2$ transitions were measured directly from the ENDOR spectra after baseline correction. For Figure 7B, the intensities for each of the four transitions measured at different concentra-

tions of bicarbonate were normalized to the intensity of the respective peak in the Mn²⁺$_{aq}$ spectra (no added bicarbonate). Because Mn²⁺$_{aq}$ has six water ligands (i.e., 12 protons) in the first coordination shell,[39] the normalized intensities in Figure 7B give a quantitative measure of the average number of water ligands (protons) per one Mn²⁺ in bicarbonate solution. We notice that the four ENDOR transitions show nearly identical dependence on bicarbonate concentration within experimental error. We interpret this as a clear indication that the relative contributions from the five EPR transitions of Mn²⁺ to the ENDOR spectrum at 3490 G do not change appreciably with bicarbonate concentration. Furthermore, these relative contributions are comparable for all three complexes involved in the bicarbonate equilibrium (eq 7), namely, Mn²⁺$_{aq}$ and the 1:1 and 1:2 complexes. These conclusions together with the assumption that the geometry of the remaining water ligands in the first shell of Mn²⁺ is not appreciably affected upon bicarbonate complexation allow us to formulate a simple model to describe the dependence of the ENDOR peak intensity on bicarbonate concentration

$$p_{av}(c) = \sum_{i=0}^{2} n_i(c) \cdot p_i \tag{9}$$

where, p_i is the number of water ligand protons in each complex involved in the equilibrium ($p_0 = 12$ for Mn²⁺$_{aq}$), and $n_i(c)$ is the mole fraction for each complex as a function of bicarbonate concentration, c. To calculate $n_i(c)$, we used the equilibrium model of eq 7 and the binding constants K_1 and K_2 obtained from the room-temperature EPR and electrochemistry data (Table 1). This leaves only two fitting parameters, p_1 and p_2. Fitting of the four dependences in Figure 7B using the same set of parameters results in $p_1 = 8-10$ protons (4−5 water ligands) for the 1:1 complex and $p_1 = 4-6$ protons (2−3 water ligands) for the 1:2 complex. On the basis of these numbers, we formulate the 1:1 complex as [Mn²⁺(HCO₃⁻)(OH₂)₄₋₅] and the 1:2 complex as [Mn²⁺(HCO₃⁻)₂(OH₂)₂₋₃].

## IV. Discussion

Stability Constants of the Mn²⁺ Complexes. The observed changes in redox potential (Figure 1A and B) of the Mn²⁺/Mn⁰ couple in the presence of bicarbonate is rationalized by the formation of two electroactive Mn−bicarbonate complexes with metal/ligand stoichiometries of 1:1 and 1:2, respectively. The 1:1 complex forms at bicarbonate concentrations between 10 and 75 mM, and a 1:2 complex dominates in solution above 100 mM bicarbonate. This speciation was also confirmed in room-temperature EPR measurements (Figure 2A). Both methods resulted in stability constants in agreement with each other (Table 1) with $K_1 = 18$ M⁻¹ and $K_2 = 568$ M⁻². These constants are in good agreement with $K_1 = 18.6$ M⁻¹ for the 1:1 complex [Mn(HCO₃)]⁺ determined by potentiometric titrations at 298 K[19] and with $K_1 = 63$ and 2.8 M⁻¹ measured at 298 K at different ionic strengths of solution equal to 3.0 and 0.0, respectively.[36] The value of K_2 has never been reported before.

Binding Modes and Local Structure. The ¹³C hyperfine tensor resolved from ESEEM, ENDOR, and HYSCORE spectra unequivocally show that Mn²⁺ forms first coordination shell complexes with bicarbonate/carbonate. The simulation parameters (Table 2) can be used to infer the local structure and specifically the binding modes of carbonate ligand in the coordination sphere of Mn²⁺.

The anisotropic part of the ¹³C hyperfine tensor ($T = 0.8$ MHz) may involve two contributions: a direct dipole−dipole

SCHEME 1: Deduced Structure of the 1:2 Complex, $Mn^{2+}(CO_3^{2-})(HCO_3^-)(OH_2)_3$, Formed in Solution at High Bicarbonate Concentrations (>50 mM) at pH 8.3[a]
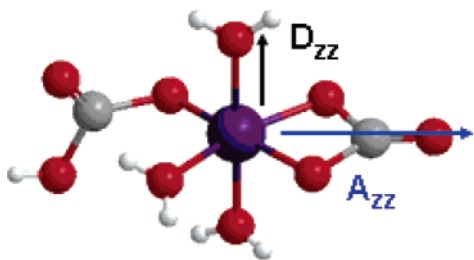
^{a} The arrows (D_{ZZ} and A_{ZZ}) show orientations of the principal axes of ZFS and ^{13}C hyperfine coupling tensors. Their relative angle 90° corresponds to angle β derived from ^{13}C HYSCORE simulations.

hyperfine interaction (T_{dd}) between the ^{13}C nucleus and the unpaired electron spin residing on Mn^{2+} and also the anisotropic term (T_p) arising from the finite electron spin density localized on the p orbital of the bicarbonate ligand. The isotropic coupling extracted from our simulations, $a_{iso} = -1.1$ MHz, corresponds to about 3% of the unpaired electron spin density on the p orbital of the bicarbonate ligand as can be estimated based on $a_{iso} \approx 33$ MHz reported for 100% spin density localized on the p orbital of the (bi)carbonate radical in solutions.[46] This 3% of p-orbital spin density translates into $T_p = 0.09$ MHz as estimated using the value $T_p = 3$ MHz reported for the carbonate radical anion.[47] Assuming that the main axes of the two anisotropic tensors (T_{dd} and T_p) are oriented by 90° to each other (as might be expected for the complex geometry shown in Scheme 1), the actual value of the dipole−dipole term can then be estimated, $T_{dd} = 0.85$ MHz. This later value can be used in a point-dipole approximation to estimate the distance (R) between the electron spin density localized on Mn^{2+} ion and the ^{13}C nucleus of the bound (bi)carbonate ligand

$$T_{dd} = \frac{g_e\beta_e\, g_n\beta_n}{hR^3} \qquad (10)$$

Here all parameters are as defined above for eq 1. In the case of ^{13}C, this equation reduces to $T = 19.9/R^3$ (in MHz), where R is in Å. Thus, $T_{dd} = 0.85 \pm 0.1$ MHz derived from the spectral simulations corresponds to a distance of 2.85 ± 0.1 Å between the Mn^{2+} and ^{13}C nuclei.

Carbonate complexes of 3d transition-metal ions have been synthesized previously, and their X-ray structures have been resolved (reviewed in ref 48). It has been shown that (bi)-carbonate can bind in either monodentate or bidentate modes, and the average distances (Mn−C) for both types of coordination are summarized in Table 3. No distances have been reported for Mn^{2+}−bicarbonate complexes although a distance of 3.048 Å for a bridging bicarbonate in polymeric $MnCO_{3(s)}$ has been observed.[49] For other transition metal ions, for example, Cu^{2+} and Co^{2+}/Co^{3+}, the metal−carbon distances are known for both monodentate and bidentate coordination modes (Table 3). Co^{2+} usually exhibits a monodentate coordination, whereas Co^{3+} prefers a bidentate coordination. Cu^{2+} was observed in both mono- and bidentate coordination modes. Limited EPR data are available on Cu^{2+}−bicarbonate complexes in solutions and demonstrate comparable metal−carbon distances to what is found in single crystals.[50] On the basis of the Cu^{2+}−C and Co^{2+}/Co^{3+}−C distances and renormalizing for a greater ionic radius of Mn^{2+} (see footnote b of Table 3), we estimated the expected Mn−C distances of 2.75−2.9 Å for a bidentate coordination of bicarbonate to Mn^{2+} and 3.3−3.35 Å for a monodentate

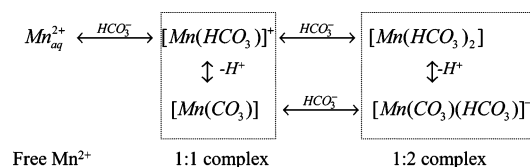**TABLE 3: X-ray Distances for Metal−(Bi)carbonate Complexes[a]**

r(metal-^{13}C) in carbonate modes	(Cu−^{13}C) Å	(Co−^{13}C) Å	(Mn−^{13}C) Å
monodentate	2.9[b]	3.1[c]	3.35[d]
bidentate	2.4−2.5[b]	2.3−2.4[c]	2.75−2.9[d]
			2.75−2.95 (this work)

^{a} Both mono- and bidentate coordination modes are included. ^{b} On the basis of X-ray diffraction on single crystals of copper complexes: $[Cu(HCO_3)]_{(aq)}$, $[Cu(CO_3)]_{(aq)}$, $[Cu(CO_3)_2]^{2-}_{(aq)}$, and $Na_2[Cu(CO_3)_2]_{(s)}$.[50] ^{c} On the basis of X-ray diffraction on single crystal of cobalt complexes: $K_2[Co^{II}(H_2O)_4(CO_3)_2]_{(s)}$ for monodentate, $[Co^{III}(NH_3)_4CO_3]Br_{(s)}$ for bidentate.[48] ^{d} Estimated based on ionic radii ($Co^{3+} = 0.63$ Å, $Co^{2+} = 0.74$ Å, $Cu^{2+} = 0.69$ Å, and $Mn^{2+} = 0.80$ Å).

coordination. It is concluded that the distance 2.85 ± 0.1 Å derived from our EPR data for one of the (bi)carbonate ligands in the 1:2 complex corresponds to the bidentate coordination. The bidentate mode of coordination invokes a π-type overlap between the $2p_\pi$ orbital of the carbonate ligand and two d_π orbitals (d_{zx} and d_{zy}) of Mn^{2+}. Thus, a significant transfer of unpaired electron spin density from Mn^{2+} onto the (bi)carbonate ligand can be expected that explains the substantial isotropic hyperfine coupling, $a_{iso} = 1.1$ MHz, found on the ^{13}C nucleus. To our best knowledge, the bidentate coordination has never been identified previously in aqueous solution speciation of Mn^{2+}.

Upon comparing the experimental and simulated ESEEM intensities (Figure S4A), we concluded that the resolved ^{13}C coupling belongs to one (bi)carbonate ligand in the 1:2 complex and that the second bicarbonate ligand is EPR-invisible. We thus speculate that this second ligand probably coordinates in a different (monodentate) mode and its poor spectral resolution is explained by either a small hyperfine coupling or by a large dispersion (strain) in the hyperfine tensor rendering the nuclear spin transitions to be broad and unobservable (e.g., the disappearance of the proton combination line was reported in ESEEM spectra of Mn^{2+}_{aq}).[29] The ^{1}H ENDOR data supports this model by revealing that there are three water ligands in the first coordination shell of Mn^{2+} in the 1:2 complex. Having three water ligands leaves only three coordination sites on Mn^{2+} to bind two (bi)carbonate ligands. Two of these sites are occupied by the first carbonate ligand bound in bidentate mode. The second bicarbonate thus binds to the remaining vacant binding site in a monodentate coordination mode.

Our suggested structure for the 1:2 complex is shown in Scheme 1. This involves two (bi)carbonate ligands, one in bidentate and the second in monodentate mode, and three water ligands. We assume a trans relative position for the two (bi)-carbonate ligands (not known directly from our simulations), yielding a facially ligated pseudo-octahedral complex. The arrows show the orientations of the principal axes of the ZFS tensor (D_{ZZ}) and also the ^{13}C hyperfine tensor (A_{ZZ}) for the bidentate bicarbonate ligand in the molecular frame of the complex. The hyperfine tensor arises from dipole electron−nuclear spin interaction, and its principal axis (A_{ZZ}) lies along a vector connecting Mn^{2+} to the ^{13}C nucleus of the ligand. The ZFS tensor arises from noncubic distortions to the Mn^{2+} ligand field, and therefore the ZFS principal axis (D_{ZZ}) should lie oriented along the main symmetry axis of the ligand field. (Bi)-carbonate ions are known to be a stronger ligand than H_2O molecules, and therefore for the structure shown in Scheme 1 the two (bi)carbonate ligands define the plane of the strongest distortion to the ligand field symmetry of Mn^{2+}. The symmetry axis of the ligand field (and thus the orientation of the principal

SCHEME 2: Model Describing Speciation Equilibrium of Mn^{2+} in Bicarbonate Solutions at pH 8.3

$$Mn_{aq}^{2+} \xleftarrow{HCO_3^-} [Mn(HCO_3)]^+ \xleftarrow{HCO_3^-} [Mn(HCO_3)_2]$$

$$\updownarrow -H^+ \qquad\qquad \updownarrow -H^+$$

$$[Mn(CO_3)] \xleftarrow{HCO_3^-} [Mn(CO_3)(HCO_3)]^-$$

Free Mn^{2+} 1:1 complex   1:2 complex

axis of ZFS) should be perpendicular to the plane as is shown with arrow in Scheme 1. With this arrangement, the principal axes of ZFS tensor (D_{ZZ}) and the ^{13}C hyperfine tensor (A_{ZZ}) form a 90° angle, which is consistent with $\beta = 90°$ derived from the HYSCORE spectral simulations.

Mn^{2+} Speciation Model and its Significance. Scheme 2 shows the chemical speciation of Mn^{2+} in aqueous bicarbonate solutions as inferred from the data presented in this work. The room-temperature electrochemistry and EPR data reveal the presence of 1:1 and 1:2 complexes in solution. The 1:1 species formed in the concentration range of 10−50 mM bicarbonate is represented in Scheme 2 by two species, $[Mn(HCO_3)]^+$ and $[MnCO_3]$, for example, bicarbonate and carbonate forms of the complex. The existence of two (protonated and deprotonated) forms can be rationalized as follows. The pK_a of free bicarbonate ion in solution is 10.5. The pK_a of bicarbonate bound to Mn^{2+} is unknown but expected to be significantly lower because of the electropositive nature of Mn^{2+}. Upon binding to Mn^{2+} the pK_a of the water molecule is decreased by 5 units, from 15.6 to 10.5. Taking into account the negative charge on the bicarbonate molecule, one expects a smaller effect (decrease by 2−3 units) compared to a water molecule. The stability constants for the 1:1 Mn−bicarbonate and Mn−carbonate complexes have been measured[48] and can be used to estimate p$K_a \approx 8.5$ for bicarbonate bound to Mn^{2+}. Thus at pH = 8.3 used in our electrochemistry and EPR experiments both bicarbonate and carbonate complexes are expected at comparable fractions. Similarly, the 1:2 species in Scheme 2 is also represented by the equilibrium of $[Mn(HCO_3)_2]$ and $[Mn(CO_3)(HCO_3)]^-$ considering the deprotonation of one of the bound bicarbonate ligands. Thus, the overall Mn^{2+} speciation is represented by the equilibrium of five species and their population depends on the bicarbonate concentration and pH of the solution.

The speciation shown in Scheme 2 is important for understanding the redox chemistry of Mn^{2+} in aqueous solutions. The oxidation potentials (in Mn^{2+}/Mn^{3+} redox couple) for the 1:1 and 1:2 Mn−bicarbonate complexes have been found to decrease significantly from $E^0 = 1.18$ V for Mn_{aq}^{2+} to 0.67 and 0.52 V, respectively.[21] These low oxidation potentials bring these bicarbonate complexes well within the range of oxidation capability of many metalloenzymes, like photosystem II. Thus formation of the Mn^{2+}−bicarbonate complexes might have important implication for biological oxidation pathways of Mn^{2+}. An important example is found in the field of photosynthesis. The photopigments of the native reaction centers from *Rhodobacter sphaeroides*, a class of anoxygenic phototrophs, have a redox potential close to 0.5 V, which can be raised slightly to 0.6−0.7 V by selective mutation of the residues near the reaction center.[14] These potentials are not high enough to oxidize Mn_{aq}^{2+} (1.18 V). However, it has been shown that the redox potential of the mutant is already sufficiently high to allow oxidation of Mn^{2+}−bicarbonate complexes that have potentials of 0.55−0.6 V. This work has demonstrated unequivocally that upon formation of Mn^{2+}−bicarbonate complexes, Mn^{2+} becomes available for a broader range of biological reactions.

Another important example is the photoassembly process of

the Mn_4 cluster in PSII-WOC. A previous study has shown that the bicarbonate anion plays a selective role in enhancing the rate of assembly of the inorganic Mn_4 core responsible for oxygen evolution activity during biogenesis and repair of PSII-WOC. In vitro studies indicate that presence of bicarbonate ($\sim$1 mM) leads to a fourfold acceleration of the net rate of light-induced photooxidation of the first Mn^{2+} by apoWOC-PSII and an increase in the yield of reconstituted centers owing to reduction of photoinhibition.[8] Formation of a ternary Mn^{2+}−bicarbonate−apoPSII complex (with a low oxidation potential) appears to be the origin of the increased assembly rate of the cluster in the presence of bicarbonate.[51]

The Mn^{2+}−bicarbonate complexes have also been hypothesized to play an important role in the evolutionary origin of oxygenic photosynthesis in the archean era.[12,52] At highly elevated bicarbonate concentrations in the archean ocean, the speciation of many polyvalent metal ions was largely shifted in favor of metal$_x$−(bi)carbonate$_y$ complexes. The low pH of the archean ocean prevented the precipitation of insoluble metal−carbonate/hydroxide minerals, thus leading to increased concentration of the metal−bicarbonate complexes in solution. The favorable oxidation potentials of the resulting Mn−bicarbonate species would have enabled them to serve as possible electron donors to early photosynthetic prokaryotes.

The present work on Mn^{2+} bicarbonate speciation clearly rules out the earlier speculations of Mn^{2+} dimeric complexes in bicarbonate solutions.[20,53] Although the pseudo-catalase activity rate was observed to be proportional to the square of Mn^{2+} concentration, this could probably be explained by either a transient dimeric complex or an outer-sphere interaction of two monomeric species in the rate-determining step of peroxide degradation. Our spectroscopic study does not support the existence of a preformed dimanganese (II, II) complex in solution.

V. Conclusions

Electroreduction and EPR spectroscopy have provided a self-consistent description of the chemical speciation of Mn^{2+} with bicarbonate in aqueous solution. The speciation involves two complexes with Mn^{2+}/bicarbonate stoichiometries of 1:1 and 1:2; their stability constants have been determined. The molecular structure of ^{13}C-labeled complexes has been studied using ESEEM, ENDOR, and 2D HYSCORE. The derived structures are $Mn^{2+}(HCO_3^-)(OH_2)_{4-5}$ for the 1:1 complex and Mn^{2+}-$(CO_3^{2-})(HCO_3^-)(OH_2)_3$ for the 1:2 complex.

Abbreviations

CW	continuous wave
EPR	electron paramagnetic resonance
ENDOR	electron−nuclear double resonance
ESEEM	electron spin echo envelope modulation
HYSCORE	hyperfine sublevel correlation spectroscopy
RT	room temperature
XRD	X-ray diffraction
ZFS	zero field splitting

Supporting Information Available: Seven additional figures are provided: dependence of Mn^{2+} reduction current on

Mn^{2+} Speciation in Aqueous Solutions of Carbonate

J. Phys. Chem. B, Vol. 110, No. 10, 2006 **5111**

Mn^{2+} concentration; Mn^{2+} EPR spectra in frozen solution at 77 K and the concentration dependence at the g 4.0 signal; comparison of the Mn^{2+} EPR data at room temperature and 77 K; two-pulse ESEEM time- and frequency-domain simulations; water stoichiometry derived from ^{1}H ENDOR spectra; additional simulations of the 2D-HYSCORE data; and a stacked plot of the experimental and simulated HYSCORE spectra. This material is available free of charge via the Internet at http://pubs.acs.org.

References and Notes

(1) Stumm, W.; Morgan, J. J. *Aquatic Chemistry*, 3rd ed.; Wiley-Interscience: New York, 1996.

(2) Martin, W.; Russell, M. J. *Philos. Trans. R. Soc. London, Ser. B* **2003**, *358*, 59.

(3) Ramirez, D. C.; Mejiba, S. E. G.; Mason, R. P. *J. Biol. Chem.* **2005**, *280*, 27402.

(4) Ferreira, K. N.; Iverson, T. M.; Maghlaoui, K.; Barber, J.; Iwata, S. *Science* **2004**, *303*, 1831.

(5) Blankenship, R. E. *Molecular Mechansims of Photosynthesis*; Blackwell Science: Oxford, U.K., 2002.

(6) Stemler, A. J. *Photosynth. Res.* **2002**, *73*, 177.

(7) Klimov, V. V.; Baranov, S. V. *Biochim. Biophys. Acta* **2001**, *1503*, 187.

(8) Baranov, S.; Tyryshkin, A.; Katz, D.; Dismukes, G.; Ananyev, G.; Klimov, V. *Biochemistry* **2004**, *43*, 2070.

(9) Biesiadka, J.; Loll, B.; Kern, J.; Irrgang, K. D.; Zouni, A. *Phys. Chem. Chem. Phys.* **2004**, *6*, 4733.

(10) Kamiya, N.; Shen, J. R. *Proc. Natl. Acad. Sci. U.S.A.* **2003**, *100*, 98.

(11) Ananyev, G. M.; Nguyen, T.; Putnam-Evans, C.; Dismukes, G. C. *Photochem. Photobiol. Sci.*, in press, 2005.

(12) Dismukes, G. C.; Klimov, V. V.; Baranov, S. V.; Kozlov, Y. N.; Dasgupta, J.; Tyryshkin, A. M. *Proc. Natl. Acad. Sci. U.S.A.* **2001**, *98*, 2170.

(13) Russell, M. J.; Hall, A. J. *Geochem. News* **2002**, *113*, 6.

(14) Kalman, L.; LoBrutto, R.; Allen, J. P.; Williams, J. C. *Biochemistry* **2003**, *42*, 11016.

(15) Thielges, M.; Uyeda, G.; Camara-Artigas, A.; Kalman, L.; Williams, J. C.; Allen, J. P. *Biochemistry* **2005**, *44*, 7389.

(16) Schallreuter, K. U.; Moore, J.; Wood, J. M.; Beazley, W. D.; Gaze, D. C.; Tobin, D. J.; Marshall, H. S.; Panske, A.; Panzig, E.; Hibberts, N. A. *J. Invest. Derm. Symp. Proc.* **1999**, *4*, 91.

(17) Liochev, S. I.; Fridovich, I. *Proc. Natl. Acad. Sci. U.S.A.* **2004**, *101*, 12485.

(18) Fouillac, C.; Criaud, A. *Geochem. J.* **1984**, *18*, 297.

(19) Lesht, D.; Bauman, J. E. J. *Inorg. Chem.* **1978**, *17*, 3332.

(20) Sychev, A. Y.; Isac, V. G. *Russ. Chem. Rev.* **1993**, *62*, 279.

(21) Kozlov, Y. N.; Zharmukhamedov, S. K.; Tikhonov, K. G.; Dasgupta, J.; Kazakova, A. A.; Dismukes, G. C.; Klimov, V. V. *Phys. Chem. Chem. Phys.* **2004**, *6*, 4905.

(22) Tan, X. L.; Bernardo, M.; Thomann, H.; Scholes, C. P. *J. Chem. Phys.* **1993**, *98*, 5147.

(23) Coffino, A. R.; Peisach, J. *J. Magn. Reson., Ser. B* **1996**, *111*, 127.

(24) Tan, X. L.; Bernardo, M.; Thomann, H.; Scholes, C. P. *J. Chem. Phys.* **1995**, *102*, 2675.

(25) Halkides, C. J.; Bellew, B. F.; Gerfen, G. J.; Farrar, C. T.; Carter, P. H.; Ruo, B.; Evans, D. A.; Griffin, R. G.; Singel, D. J. *Biochemistry* **1996**, *35*, 12194.

(26) Astashkin, A. V.; Feng, C. J.; Raitsimring, A. M.; Enemark, J. H. *J. Am. Chem. Soc.* **2005**, *127*, 502.

(27) Ross, R. T. *J. Chem. Phys.* **1965**, *42*, 3919.

(28) Kozlov, Y. N.; Kazakova, A. A.; Klimov, V. V. *Biol. Membr.* **1997**, *14*, 93.

(29) Astashkin, A. V.; Raitsimring, A. M. *J. Chem. Phys.* **2002**, *117*, 6121.

(30) Bond, A. M. *Modern Polarographic Methods in Analytical Chemistry*; Marcel Dekker: New York, 1983.

(31) Liang, C. C. In *Encyclopedia of Electrochemistry of the Elements*; Bard, A. J., Ed.; Marcel Dekker: New York, 1973; p 351.

(32) Kolthoff, I. M.; Lingane, J. J. *Polarography*; Interscience Publishers: New York, 1941.

(33) Komula, W.; Galus, Z. *Rocz. Chem.* **1962**, *36*, 1223.

(34) Biernat, J.; Korita, J. *Collect. Czech. Chem. Commun.* **1960**, *25*, 38.

(35) DeFord, D. D.; Hume, D. N. *J. Am. Chem. Soc.* **1951**, *73*, 5321.

(36) Smith, R. M.; Martell, A. E. *Critical Stability Constants*; Plenum: New York, 1976; Vol. 4: Inorganic Complexes.

(37) Abragam, A.; Bleaney, B. *Electron Paramagnetic Resonance of Transition Ions*; Dover Publications: New York, 1986.

(38) Niccolai, N.; Tiezzi, E.; Valensin, G. *Chem. Rev.* **1982**, *82*, 359.

(39) Richens, D. T. *Chemistry of Aqua Ions*; Wiley: Chichester, U.K., 1997.

(40) Khangulov, S. V.; Pessiki, P. J.; Barynin, V. V.; Ash, D. E.; Dismukes, G. C. *Biochemistry* **1995**, *34*, 2015.

(41) Dikanov, S. A. In *New Advances in Analytical Chemistry*; Atta-ur-Rahman, Ed.; Harwood Academic Publishers: Amsterdam, 2000

(42) Dikanov, S. A.; Bowman, M. K. *J. Magn. Reson., Ser. A* **1995**, *116*, 125.

(43) Dikanov, S. A.; Tsvetkov, Y. D. *Electron Spin−Echo Envelope Modulation (ESEEM) Spectroscopy*; CRC Press: London, 1992.

(44) Spoyalov, P.; Samoilova, R. I.; Tyryshkin, A. M.; Dikanov, S. A.; Liu, B.; Hoff, A. J. *J. Chem. Soc., Perkin Trans.* **1992**, *9*, 1519.

(45) Manikandan, P.; Carmieli, R.; Shane, T.; Kalb, A. J.; Goldfarb, D. *J. Am. Chem. Soc.* **2000**, *122*, 3488.

(46) Bonini, M. G.; Radi, R.; Ferrer-Sueta, G.; Ferreira, A. M. D.; Augusto, O. *J. Biol. Chem.* **1999**, *274*, 10802.

(47) Chantry, G. W.; Horsfield, A.; Morton, J. R.; Whiffen, D. H. *Mol. Phys.* **1962**, *5*, 589.

(48) Palmer, D. A.; Vaneldik, R. *Chem. Rev.* **1983**, *83*, 651.

(49) Maslen, E. N.; Streltsov, V. A.; Streltsova, N. R.; Ishizawa, N. *Acta Crystallogr., Sect. B* **1995**, *B51*, 929.

(50) Schosseler, P. M.; Wehrli, B.; Schweiger, A. *Inorg. Chem.* **1997**, *36*, 4490.

(51) Dasgupta, J.; Tyryshkin, A. M.; Baranov, S. V.; Dismukes, G. C., unpublished results.

(52) Dismukes, G. C.; Blankenship, R. E. The Origin and Evolution of Photosynthetic Oxygen Production. In *Photosystem II-The Light-Driven Water: Plastoquinone Oxidoreductase*; Wydrysinki, T., Satoh, K., Eds.; Springer: The Netherlands, 2005; Vol. 22, pp 683−695.

(53) Stadtman, E. R.; Berlett, P. B.; Chock, P. B. *Proc. Natl. Acad. Sci. U.S.A.* **1990**, *87*, 384.

(54) Inert salts such as NaNO$_3$ and KNO$_3$ are often used as alternative glass forming agents for aqueous solutions, but we found that these salts do not yield good glasses even at saturating 2M concentrations unlike other metal−carbonate systems.[26]

(55) In the ESEEM experiment at 3490 G, all five electron spin transitions within the $S = 5/2$ manifold of Mn^{2+} are excited (however, with different weights) and therefore the nuclear spin transitions from all six electron spin manifolds ($M_S = \pm 1/2$, $\pm 3/2$, and $\pm 5/2$) are expected to show up in the ESEEM spectrum.[22] However, only the nuclear transitions from $M_S = \pm 1/2$ are usually observed because the other four transitions from $M_S = \pm 3/2$ and $\pm 5/2$ are broader and therefore less intense (by factor 3 and 5, respectively).[29] Also, their weighting factors are much smaller than those for $M_S = \pm 1/2$ transitions because only part of the broad line width of the transitions involving high M_S states is excited by the microwave pulses.